THE JOURNAL OF PHYSICAL CHEMISTRY C
A JOURNAL OF THE AMERICAN CHEMICAL SOCIETY

pubs.acs.org/JPCC

Article

Fabrication and Characterization of High-Quality Epitaxial Nanocolumnar Niobium Films with Abrupt Interfaces on YSZ(001)

C. V. Ramana,* Nanthakishore Makeswaran, Vishal Zade, Debabrata Das, Susheng Tan, Shuozhi Xu, and Irene J. Beyerlein

Cite This: *J. Phys. Chem. C* 2022, 126, 2098−2107

Read Online

ABSTRACT: Niobium (Nb) is a promising refractory metal with a wide variety of technological applications in nanoelectronics, optoelectronics, photonics, and energy-related technologies. However, to further advance the field of nanoelectronics and nanophotonics, very high-quality Nb films with excellent structural order are needed. While much progress has been made in understanding the heteroepitaxy of Nb on oxide substrates, the underlying fundamental mechanisms, especially to realize films showing abrupt interfaces with the substrate and without needing the expensive equipment and/or processing under extreme conditions, remain a challenge. In this context, herein, we demonstrate an approach to stabilize the epitaxial, nanocolumnar bcc Nb films with highly ordered and abrupt interfaces on YSZ(001) substrates using simple and industrially widely adopted sputter deposition. 90 nm Nb films deposited onto YSZ(001) at 500 °C exhibit a strained, epitaxial structure. As evidenced in X-ray diffraction and transmission electron microscopy analyses, the structural quality of Nb films is driven by substrate-assisted selective nanocrystallization. Coupled with granular morphology and high structural quality, the optical properties measured by spectroscopic ellipsometry and reflectivity indicate highly reflective Nb films with enhanced optical constants. Corroborated with surface/interface quality, microstructure, and optical properties, the epitaxial Nb films exhibit excellent mechanical characteristics. The hardness and elastic modulus of the Nb epitaxial films were 18 and 240 GPa, respectively, which are attributed primarily to the growth of a compact nanocolumnar Nb epitaxial film on YSZ.

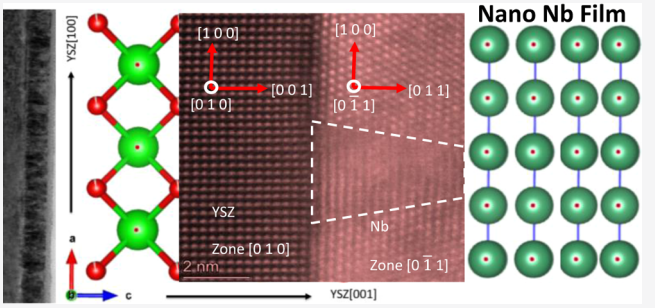

INTRODUCTION

Manipulation of the phase, structure, properties, and phenomena at the nanoscale dimensions is critical to realize the full potential of electronic and photonic materials in many of today's advanced technologies. In particular, highly ordered or engineered heterostructured epitaxial layers are becoming highly beneficial in many scientific/technological applications, such as integrated sensors, thin-film solar cells, optical filters, microelectromechanical systems, superconducting layers, electrocaloric devices, and photonic devices.[1−11] However, engineering such ordered structures with atomic scale precision and containing layers a few nanometers in thickness requires a very detailed, fundamental understanding of the crystallography, nanostructure, surface/interface chemistry, defect chemistry, and their evolution as a function of synthesis pathway. Revealing the structure−property relationship would allow for the fine-tuning of material properties for viable electronic device applications and exploring new electronic, magnetic, optical, and optoelectronic applications.

Continuous miniaturization of multifunctional devices imposes severe restrictions on the role of component layers, especially the high-quality epitaxial metal films on various substrate materials.[12−24] The metal−substrate surface/interface engineering and quality control become extremely crucial to achieve enhanced device performance. On the other hand, various parasitic characteristics of metal films, such as intermixing, chemical inhomogeneity, structural deformation, localized agglomeration of active metallic layers, diffused interface, crystalline defects, interfacial trap states, random orientation of nanocrystals, and so forth, deviate the overall performance of the electronic, photonic, magnetic, and optoelectronic devices.[12−24] Therefore, epitaxial growth of thin metal films on a wide range of semiconductor and dielectric substrates has been the topic of intense research, which spans both fundamental and applied perspectives. Furthermore, such degenerative identities are not only limited to a specific group of metals, such as refractory metals in this

Received: October 5, 2021
Revised: December 3, 2021
Published: January 20, 2022

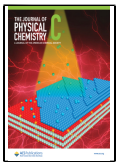

https://doi.org/10.1021/acs.jpcc.1c08738
J. Phys. Chem. C 2022, 126, 2098−2107

case, but noted for a wide range of metals for advanced magnetic, electronic, photonic, and optoelectronic device applications.[12,15−18,21,22,24] Researchers have tried various strategies to overcome these detrimental effects. Using interlayers, surface functionalization, diffusion barriers, kinetic barriers, and interface energy minimization are some of the approaches that exist in the literature.[12,17−25] For instance, Uekubo et al. used an ultrathin WN_x diffusion barrier layer to improve Cu connections on Si-based VLSI circuits.[17] Ramana et al. proposed and demonstrated using few monolayers of Ti as an interlayer to promote epitaxial growth of magnetic Fe films on nonmagnetic metals.[12] Ishibe et al. used precisely controlled growth of the $Fe_3O_4/GeO_x/Ge$ nanocrystalline interface to demonstrate a novel synaptic memory device on the Si platform.[24] Although the aforementioned growth processes are cost-effective, there are reports using highly sophisticated epitaxial growth of metallic films, both at low and high substrate temperature, for electronic, optoelectronic, and plasmonic applications. Researchers have also demonstrated epitaxial quality metallic films using the van der Waal growth technique.[23] Although it is very challenging to grow epitaxial metallic films, with superior structural, chemical, and functional quality, on various platforms, scientists and technologists have successfully demonstrated the same exploiting various novel strategies.

Niobium (Nb), a refractory metal, exhibits many mechanical, thermal, thermochemical, and electrical properties useful for a number of modern technological applications.[1,3−5,7,26] Nb and Nb-based alloys currently dominate several aerospace, defense, electronics, and energy sectors.[27−31] Due to its high melting point of 2477 °C, Nb is used in many engineering systems exposed to thermal and mechanical loadings. Nb also exhibits excellent physical and mechanical qualities. Its relatively low density, high Young's modulus, and high yield strength, which are 8.6 g cm^{-3}, 103 GPa, and 240−550 N mm^{-2}, respectively, combined with its electronic properties, make Nb and Nb-based alloys suitable for applications, where materials and devices are often subjected to extreme environments, especially, elevated temperature or pressure or radiation or combination of these.[10,27−30] Unlike other refractory metals, Nb finds widespread applications in nanoelectronics and nanophotonics. Nb thin films and nanomaterials are popular for their utilization in nano-SQUID circuits for switches operating at high frequency under cryogenic conditions, superconductivity, single photon detectors, and high-temperature plasmonic applications.[32] In addition to traditional structural and electronic device applications, recently, Nb-based multicomponent alloys have the focus of intense research in the field of design and development of advanced, refractory high-entropy alloys (RHEAs) for utilization in energy and aerospace applications.[31] While the field of RHEAs is relatively young, Nb-based RHEAs are expected to fulfil the requirements of next-generation high-temperature structural materials for operation in extreme environments. Thus, the nanostructuring of Nb and further understanding of the Nb-oxide heterostructures[33−35] are important to design materials for the current and emerging technological applications.

With continuous miniaturization of electronic, optoelectronic, photonic, and spintronic devices, the low-dimensional superconducting interconnects have become the center of interest for various overlapping multidimensional research activities. Moreover, understanding and tailoring the phase formation, chemical stability, nanomechanical behavior, and optical properties of such refractory metal and the corresponding oxides are immensely important to demonstrate state-of-the-art technologies for futuristic applications.[36−38] An abrupt heteroepitaxial interface with the lowest possible defect formation, absence of anisotropic conductivity through different crystal orientation, less surface scattering, and lower value of bulk resistivity-mean free path product ($\rho_0\lambda$) has already proven to be the most desired characteristics of Nb as a superior superconducting material.[3,39,40] The journey of Nb as a superconducting charge carrier is relatively short. Highly sophisticated layer-by-layer epitaxial growth processes have demonstrated the existence of a sharp Nb−semiconductor junction.[2,41−44] In addition, a low-cost sputtering technique has also been certified as a potential deposition technique with a similar outcome.[39,40,45] However, optimization of growth conditions on various crystalline substrates is still considered as an open problem for further improvement. Moreover, ultrahigh vacuum reactors, such as molecular beam epitaxy, vapor phase epitaxy, and so forth, are extremely energy-intensive and exceptionally costly. Multiple predeposition heat treatment and relatively higher substrate temperature ($T_s \geq 600$ °C) have been used to demonstrate good-quality epitaxial Nb growth on various substrates. This increases the thermal budget of the whole process flow. As a result, realization and optimization of cost-effective epitaxially grown Nb thin films and nanostructures on various substrates are an open problem for the scientific and engineering research community.

Kurter et al. successfully tailored the Nb nanostructure-based superconducting metamaterial to its plasmonic limit.[3] The third order of tunability through temperature, electric field, and magnetic field makes these Nb-based nanostructures more versatile and an intense research topic for the scientific community. In addition, durability of Nb at much elevated temperature introduces it into a refractory plasmonic metasurface.[1,3−5,7] Compared with Au, the most common plasmonic material, Nb can better survive harsh environments. Combining this emerging aspect with a suitable substrate material can open up new avenues and new dimension of research for the design and development of nanoscale devices for harsh environment applications.[46] In this context, the present work was performed on Nb epitaxial structures on yttria-stabilized zirconia (YSZ) substrates. The choice of YSZ to realize high-quality, epitaxial, nanostructured Nb films is due to the following reasons. YSZ is a well-known material for a thermal barrier coating for combustion engines and similar extreme applications.[47] Evidently, direct integration of various electrical−optical sensors, actuators, transducers, controllers, and so forth, on YSZ is always being a virtue for the technological improvement.[6,8,48,49] Therefore, coupling Nb with such a widely used material for various energy and power devices has the potential for further advancements in energy and defense applications. With this motivation, we have demonstrated a low substrate temperature (500 °C) epitaxial growth of Nb on YSZ. Detailed characterization using X-ray diffraction (XRD), transmission electron microscopy (TEM), and atomic force microscopy (AFM) analyses allowed us to probe and understand the structural, interfacial, and morphological characteristics of the heteroepitaxial Nb thin film on the YSZ substrate. Furthermore, theoretical calculation has been employed to understand the strain formation at the heterointerface between Nb and YSZ. Finally, optical reflectance combined with spectroscopic ellipsometry measure-

https://doi.org/10.1021/acs.jpcc.1c08738
J. Phys. Chem. C 2022, 126, 2098−2107

ments allowed us to establish the optical quality of Nb films in addition to present the variation of optical constants (n, k) throughout a wide wavelength range (ultraviolet to near-infrared regions).

EXPERIMENTAL DETAILS

Fabrication. Nb films were deposited onto YSZ(001) substrates through the use of radio-frequency sputtering. The wafers were cleaned with acetone, ethyl alcohol, and DI water, respectively, and dried with nitrogen before placement in a vacuum chamber. The chamber was then evacuated to a base pressure of $\sim 10^{-7}$ Torr. A 2 in. diameter Nb target of 99.95% purity (Plasmaterials, Inc.) was used in conjunction with a 2 in. diameter sputter gun placed 7 cm from the substrate. A sputtering power of 40 W was initially applied to the target, while argon (40 sccm) was introduced into the chamber to ignite the plasma, with the gas flow being controlled with a mass flow meter. Once ignition was achieved, the power was increased to 100 W for the actual deposition, while the final deposition pressure was tuned to 5 mTorr. Presputtering was performed for 15 min with a shutter closed above the gun. During deposition, the temperature was fixed at 500 °C. The deposition time was set under optimum conditions, resulting in a Nb film thickness of ∼90 nm. The substrates were subjected to a constant rotation at 3−4 rpm to ensure lateral isotropy. The average measured thickness of the deposited Nb films was ∼90 nm.

Characterization. *Grazing Incidence XRD.* The samples were first characterized by grazing incidence XRD at room temperature utilizing a Bruker D8 ADVANCE system (Cu Kα radiation, and λ = 1.54 Å). To focus on the surface layer of the film, a grazing incident angle of 1° was selected for the incoming X-rays. The detector scanned between 10 and 67° with a speed of 0.5 s/step.

Transmission Electron Microscopy. TEM characterization was carried out on a Thermo Scientific (formerly FEI) Titan Themis 200 G2 probe aberration-corrected system equipped with a SuperX energy-dispersive X-ray spectrometer and operated at 200 kV. The TEM specimens were prepared using an FEI Scios focused ion beam (FIB) and scanning electron microscopy (SEM) dual-beam system following a standard protocol for TEM specimen preparation. First, using an electron beam at 5 kV, 1.6 nA, a thin carbon protection layer of 15 μm × 2 μm was deposited on the Nb film grown on he YSZ(001) substrate; then, a 15 μm × 2 μm × 2 μm Pt protection film was deposited on top of the carbon protection layer at 30 kV, 300 pA, followed by rough cutting, cleaning cut, J-cut, lamellae transfer out of the substrate to a TEM grid, and final thinning. The final thinned specimen of about 80 nm was further FIB-cleaned at 5 kV, 48 pA and 2 kV, 27 pA, respectively, to remove excess amorphotized and contaminated layer. TEM data processing, if any, was carried out using the relevant offline data processing software from Thermo Scientific. ICDD PDF-4+ was used to verify the crystallographic structures of both YSZ substrate and Nb film. Dr. Probe, software for high-resolution STEM image simulation, was employed to simulate HAADF STEM images to confirm correct structural characteristics of the YSZ substrate and Nb film.

Atomic Force Microscopy. AFM is used for surface topography and roughness analysis, which can complement cross-sectional TEM, providing understanding of the grain growth kinetics of the Nb sputtered on YSZ at 500 °C. Trax NaioAFM was used with standard commercial tips both in the tapping and contact mode (ASPIRE—CT170, CCS) with spring constants at 50 and 0.1 N/m, respectively. The data were acquired in an ambient atmosphere with standard raster scanning across the the thin-film surface to acquire topographic information.

Ellipsometry. Spectroscopic ellipsometry was utilized to find the optical properties and surface/interface characteristics of the Nb coatings. Δ and ψ (phase difference and amplitude component) were determined using a Semilab S3-2000 vertical variable-angle spectroscopic ellipsometer (Semilab Semiconductor Physics Laboratory Co. Ltd, Budapest, Hungary). Measurements were carried out over a wavelength range of 300−1200 nm at 300 K in air and using 60, 65, and 70° for the angles of incidence in measurement. Post analysis of the ellipsometry data was performed using Semilab-provided analysis software.

The optical properties and microstructure of the samples can be related to the measured angles via[50]

$$\rho = R_p/R_s = \tan \Psi \exp(i\Delta) \tag{1}$$

where R_p is the complex reflection coefficients of the light polarized parallel to the plane of incidence and R_s is perpendicular to it. In order to minimize the mean-squared error, the Levenberg−Marquardt regression algorithm was used

$$\mathrm{MSE} = \frac{1}{2N - M}\sum_{i=1}^{n}\left[\left\{\frac{(\Psi_{exp} - \Psi_{calc})}{\sigma_{\Psi_i}^{exp}}\right\}^2 + \left\{\frac{(\Delta_{exp} - \Delta_{calc})}{\sigma_{\Delta_i}^{exp}}\right\}^2\right] \tag{2}$$

where Ψ_{exp}, Ψ_{calc}, and Δ_{exp}, Δ_{calc} are the measured and calculated ellipsometry functions. M represents the number of fitted parameters in the optical model, while N is the number of measured (Ψ, Δ) pairs. σ represents the standard deviation in the data. In order to factor in the optical inhomogeneity, multiple measurements were performed and analyses were carried out to calculate the level of inhomogeneity in the films. The variation in the index of refraction was $\Delta n = \pm 0.01$.

Diffuse Reflectance Spectroscopy. In accordance with spectroscopic ellipsometry, to determine intrinsic optical constants, ultraviolet−visible−near-infrared spectroscopy was performed to analyze the overall optical reflectance of the epitaxial Nb thin film on YSZ. Owing to the semitransparent nature of the YSZ substrate, spectroscopic characterization using the JASCO V-770 spectrometer was performed through the indirect diffused reflectance mode inside an integrating sphere with an inbuilt photodetector.[51]

Mechanical Properties. The mechanical property of the as-deposited Nb films was characterized using nanoindentation tests in a Hysitron T1750 Tribo nanoindenter. The intrinsic mechanical characteristics, namely, hardness (H) and reduced elastic modulus (E_r), were measured by nanoindentation measurements on Nb films using a pyramidal shape Berkovich diamond indenter. The angle between the tip axis and triangular pyramid faces was of 65.3°, whereas the effective size of the apex was about 100 nm. Standard loading and unloading curves were employed to derive the mechanical properties of Nb thin films. We employed the standard

https://doi.org/10.1021/acs.jpcc.1c08738
J. Phys. Chem. C 2022, 126, 2098−2107

methods to determine the mechanical characteristics (H and E_r), which were calculated using the method developed by Oliver and Pharr.[38,52] As described in our previous reports,[38,52] E_r can be derived by characterizing the stiffness (S) of the film from the slope of the unloading curve using the following relation between E_r and S

$$E_r = \frac{\sqrt{\pi}}{2}\frac{S}{\sqrt{A}} \tag{3}$$

where A is defined as the area of contact at peak load. To find the hardness values, the same value for the area of contact is used along with the maximum load (P_{max}) in

$$H = \frac{P_{max}}{A} \tag{4}$$

RESULTS AND DISCUSSION

Crystal Structure. Knowledge of the crystal structure, phase formation, interdiffusion, lattice parameters, cumulative strain, and so forth is needed before going forward with detailed characterization of any heteroepitaxial thin film or nanostructure on a foreign substrate. These parameters are the most basic structural fingerprint needed for optimizing an epitaxial growth strategy. They can also be important in situations of extreme environments, in service as superconducting, plasmonic, and optoelectronic devices. High-resolution XRD (HRXRD), complemented by cross-sectional TEM analysis and surface morphological characteristics, can depict the microscopic structural characteristics of the heteroepitaxial Nb film on the YSZ substrate.

The $\theta/2\theta$ scans for XRD measurements were obtained using a Rigaku X-ray diffractometer. The XRD parameters employed were 20−80° (2θ range), step size 0.02°, and scan rate 0.6°/min. The observations were made according to Bragg's law

$$n\lambda = 2d \sin\theta \tag{5}$$

where n, λ, d, and θ represent the order of reflection, incident X-ray wavelength, interplanar spacing, and incident X-ray angle, respectively. The interplanar spacing was calculated using the cubic system relation as follows

$$d = \frac{a}{(h^2 + k^2 + l^2)^{1/2}} \tag{6}$$

where a is the lattice constant, d is the interplanar spacing, and h, k, l are the Miller indices. The XRD scan in Figure 1 clearly reveals a prominent peak at 35.9° from the (011) plane of the cubic crystal lattice of Nb in the $Im\bar{3}m$ space group.[53] There is no evidence of XRD peaks from lattice planes other than the (011) family. This confirms the single-phase heteroepitaxial growth of Nb on the YSZ substrate.

The lower position of the (011) plane in our work, relative to prior published powder diffraction files of the same peak at 38.1°, reveals that there was a significant increase in the lattice dimension from 3.33611 to 3.35320 Å. This extended lattice structure of the Nb crystal initiated by the dimensions of the (001) plane of YSZ enables epitaxial growth at the interface with the (011) plane of the cubic Nb crystal structure. To understand the effect of lattice mismatch at the heterointerface, we have used theoretical calculations to estimate the amount of misfit stress generated inside the Nb lattice, while growing on a foreign substrate as YSZ.

Here, we estimate the coherency strain/stress in the YSZ/Nb bilayer composite. Let the z direction be the normal to the

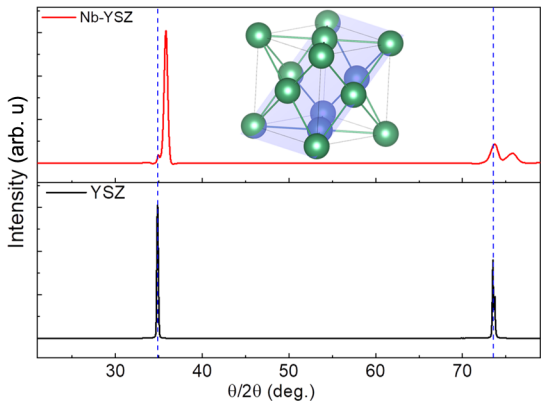

Figure 1. XRD pattern of a monocrystalline YSZ (001) substrate (bottom) and an epitaxial Nb thin film on YSZ (top). The crystalline Nb film is showing the (011)-oriented lattice plane parallel to the growth direction.

bilayer interface. The lattice parameters of YSZ and Nb are 5.125 and 3.336 Å, respectively. Within the interface, the average distance between two adjacent Y or Zr atoms in the YSZ layer is 4.374 Å and that between two adjacent Nb atoms in the Nb layer is 3.647 Å. Assuming that the YSZ layer does not deform, the misfit strain in the Nb layer is

$$\epsilon_{xx} = \epsilon_{yy} = \epsilon_{mf} = \frac{a_{YSZ} - a_{Nb}}{a_{Nb}} = \frac{4.374 - 3.647}{3.647} = 0.199 \tag{7}$$

Further assuming that the Nb film is in plane stress, $\sigma_{zz} = 0$. Then, the misfit stress is

$$\sigma_{mf} = M\epsilon_{mf} \tag{8}$$

where M is the biaxial elastic modulus. Since the normal-to-interface direction is [011], M is different along the two in-plane [100] and [0$\bar{1}$1] directions. The values of M are[54]

$$M_{[100]} = C_{11} + C_{12} - \frac{C_{12}(C_{11} + 3C_{12} - 2C_{44})}{C_{11} + C_{12} + 2C_{44}} \tag{9}$$

$$M_{[0\bar{1}1]} = \frac{C_{11} + 3C_{12} + 2C_{44}}{2} - \frac{(C_{11} + C_{12} - 2C_{44})}{2} \frac{(C_{11} + 3C_{12} - 2C_{44})}{C_{11} + C_{12} + 2C_{44}} \tag{10}$$

In Nb, substituting C_{11} = 245 GPa, C_{12} = 132 GPa, and C_{44} = 28.4 GPa in the two equations yields

$$M_{[100]} = 199.24 \text{ GPa} \qquad M_{[0\bar{1}1]} = 133.29 \text{ GPa}$$

As a result, the misfit stresses are

$$\sigma_{[100]} = 0.199 \times 199.24 = 39.69 \text{ GPa}$$

$$\sigma_{[0\bar{1}1]} = 0.199 \times 133.29 = 26.55 \text{ GPa}$$

with complementary observations from cross-sectional TEM in the next section, we can also see the tensile stress induced by YSZ causing a twist along the [011] zone axis of the Nb thin film. The cross-sectional data also show that the tensile strain is relieved periodically for a length of 4 nm after which epitaxy is restored.

Heteroepitaxial Interface. Figure 2a shows a bright-field cross-sectional TEM image of the Nb film grown on the YSZ(001) substrate taken under in-zone conditions with a YSZ

https://doi.org/10.1021/acs.jpcc.1c08738
J. Phys. Chem. C 2022, 126, 2098−2107

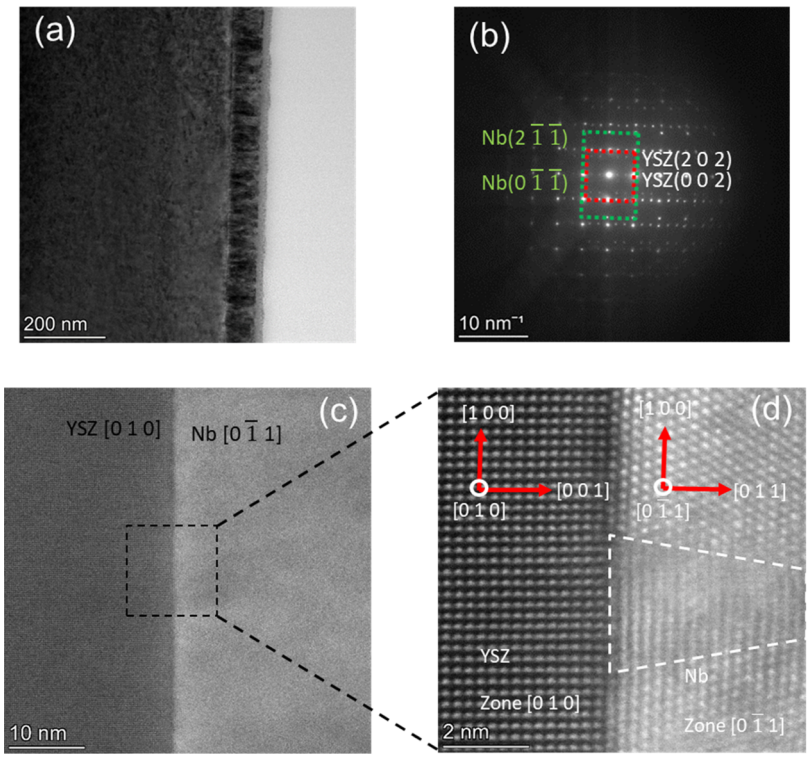

Figure 2. (a) Bright-field TEM micrograph of the cross section of Nb(011)//YSZ(001). Columnar grain structure was observed in the film. (b) Corresponding SAED pattern of the interface shows that the films exhibit single-crystal-like structure and well-defined orientation relationship between Nb and YSZ. (c) High-resolution HAADF STEM image of Nb(011)/YSZ(001) observed along a YSZ zone axis of [010]. (d) Atomic-resolution HAADF STEM image of a region at the interface of (c).

zone axis of [010]. The thickness of the Nb film is measured from the TEM image to be ∼95 nm which is further verified with spectroscopic ellipsometry analysis. Figure 2a reveals that the Nb film exhibits a single-crystal-like structure with columnar grains of the same growth orientation. The interface between the Nb film and YSZ substrate is straight and sharp without intermixing. The corresponding selected area electron diffraction (SAED) pattern is shown in Figure 2b. The specimen was tilted before the SAED pattern was captured so that the electron beam was parallel to the zone axis [010] in single-crystal YSZ(001). In the meantime, the SAED pattern shows that the zone axis of Nb[0$\bar{1}$1] is parallel to YSZ[010] and Nb(100) is parallel to YSZ(100), namely, Nb[0$\bar{1}$1]// YSZ[010] and Nb(100)//YSZ(100), a well-defined orientation relationship between the Nb film and the YSZ(001) substrate. This orientation relationship is consistent with the XRD observation, for example, Nb(011)//YSZ(001), indicating that the Nb(100) plane is rotated 45° around the Nb[100] zone axis to minimize the lattice mismatch between these two dissimilar materials during growth. Figure 2c presents a high-resolution HAADF STEM image of Nb(011)/YSZ(001) taken along the YSZ[010] zone axis, and also along Nb[0$\bar{1}$1], as they are parallel to each other. The image indicates that the interface is atomically flat and sharp without any second phase over a large area. The absence of a second phase is attributed to full immiscibility between Nb and Zr(Y). The periodic strain contrast visible along the interface is an indication of misfit dislocations.

In order to clearly observe misfit dislocations, a selected small region at the interface in Figure 2c was further imaged at atomic resolution, which is shown in Figure 2d. The atomic-resolution HAADF STEM image shows that the interface is truly straight and atomic flat and misfit dislocations spaced 3 nm apart were produced to balance the interface strain. The high-resolution STEM analysis in accordance with HRXRD data confirms the low-temperature epitaxial growth of the Nb thin film on the YSZ substrate with sharp atomically flat heterointerfaces in between. The growth front is nano-columnar with a periodic lattice twist to minimize the overall lattice strain.[55−57]

Figure 3 provides a schematic of the Nb−YSZ hetero-interfaces based on XRD and cross-sectional TEM analyses. Both 2D and 3D (Figure 3a,b) schematics clearly portray the atomic arrangement at the junction and the corresponding planes parallel to the growth direction.

Surface Morphology. The size of the AFM scan is optimized to enable accurate roughness value extraction. The root mean square roughness and average roughness values were calculated using Gwyddion software, and WSXM was used to validate calculations. Roughness analysis provides quantitative information on the effect of specific processing parameters of the Nb thin film during sputtering. Correlating the cross-sectional data with the surface topography indicates the anisotropy of the crystalline grains toward the growth direction normal to the substrate. The effect of thermal energy given to the adatoms of Nb to mobilize on the surface of YSZ during synthesis to form epitaxial interfaces is inferred clearly from TEM and AFM. The formulas used for roughness analysis are

$$R_q = \left[\left(\frac{1}{L}\right)\int_0^L Z(x)^2 \mathrm{d}x\right]^{1/2} \quad (11)$$

https://doi.org/10.1021/acs.jpcc.1c08738
J. Phys. Chem. C 2022, 126, 2098−2107

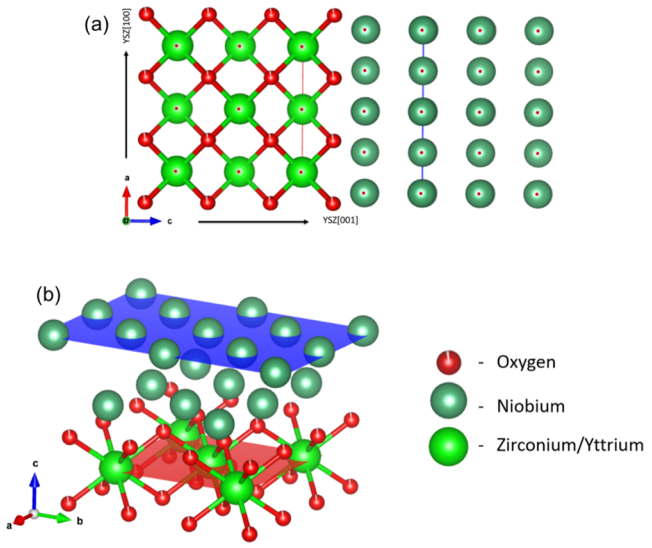

Figure 3. 2D and 3D schematic of Nb−YSZ heterointerfaces, where the blue and red planes represent Nb(011) and YSZ(001), respectively.

$$R_a = \left(\frac{1}{L}\right)\int_0^L |Z(x)|\mathrm{d}x \tag{12}$$

Figure 4a shows the microscopic morphology of the uncapped top surface of an epitaxially grown Nb thin film. The surface of the film seems to be quite flat with R_q (root mean square average of deviation) value at 1.75 nm and an R_a (average roughness) value at 1.39 nm but with clear cone structures indicating the presence of grains in the range of 50−100 nm diameter. This conical growth front with closely packed nanocolumnar epitaxial topology is beneficial for efficient light trapping and can be tailored with optimized growth kinetics. Such controlled low-temperature growth of heteroepitaxial Nb on YSZ has tremendous applicability in extreme environment transducers, sensors, and protective coating applications. In addition to this detailed structural and topological exploration, we will further investigate the optical domain to understand the photonic interaction with the subjected metallic thin film. From a technical viewpoint, the result can serve as a benchmark in designing high-temperature photonic or plasmonic devices.

Optical Properties. The refractive index (n) and extinction coefficient (k) of thin films were fitted with a Tauc−Lorentz dispersion model, while this model is more typically used to fit parameters for semitransparent and metallic oxide materials. In this trial, after comparison with a variety of other models, the Tauc−Lorentz model yielded the best fit of the data and the closest to the experimentally expected thickness values of the films. The model is given by

$$\varepsilon_{2,\mathrm{TL}}(E; A, E_0, E_g, C) = \theta(E - E_g)\frac{(E - E_g)^2 A E_0 C}{(E^2 - E_0^2)^2 + C^2 E^2}\left(\frac{1}{E}\right) \tag{13}$$

E_0 is the central energy of the oscillator, C is the oscillator width, and A is a fitting parameter. θ stands for the Heaviside function and it is +1 or 0 for photon energies above or below E_g, respectively; hence, ε_2 is zero in the TL model for energies below E_g.

Extracting meaningful physical information from ellipsometry measures requires an optical model of the sample that accounts for multiple distinct layers with different optical dispersions. In particular, the layer interfaces act as optical boundaries where light can be refracted/reflected as per the Fresnel relations. Figure 5a depicts a schematic of the Nb thin film on the YSZ substrate. Here, linearly polarized monochromatic light with precisely controlled frequency was subjected on a Nb thin film and modulation of reflected light was analyzed to extract frequency-dependent optical constants of the thin film. A study of the thicknesses of the sample shows that all depositions are achieved within 10 nm from an intended total thickness of 100 nm for the Nb films, indicating consistent deposition conditions and well-controlled parameters for the samples.

Figure 5 presents the variation in the refractive index (Figure 5b) and extinction coefficient (Figure 5c) for Nb films deposited on YSZ. It should be noted that all samples were measured accounting for the inherent surface roughness. Two important observations that can be made from the dispersion profiles of optical constants are as follows. First, for epitaxial Nb films, both n and k values increase with an increasing wavelength. In fact, the dispersion profiles noted for Nb films are in good agreement with a typical behavior expected for metallic thin films.[13,14,58] Therefore, the higher n, k values noted may be due to smaller grain size. Finally, to further confirm and validate the optical quality, the reflectivity of the Nb film surfaces is measured. Figure 5d depicts the diffused reflection data of the as-grown Nb film on the YSZ substrate.

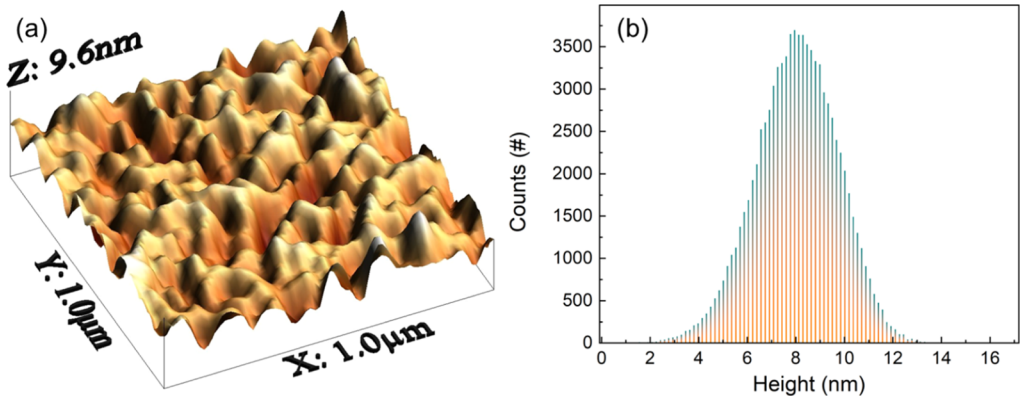

Figure 4. (a) 3D AFM image of a heteroepitaxial Nb film. (b) Surface roughness histogram of the AFM image.

https://doi.org/10.1021/acs.jpcc.1c08738
J. Phys. Chem. C 2022, 126, 2098−2107

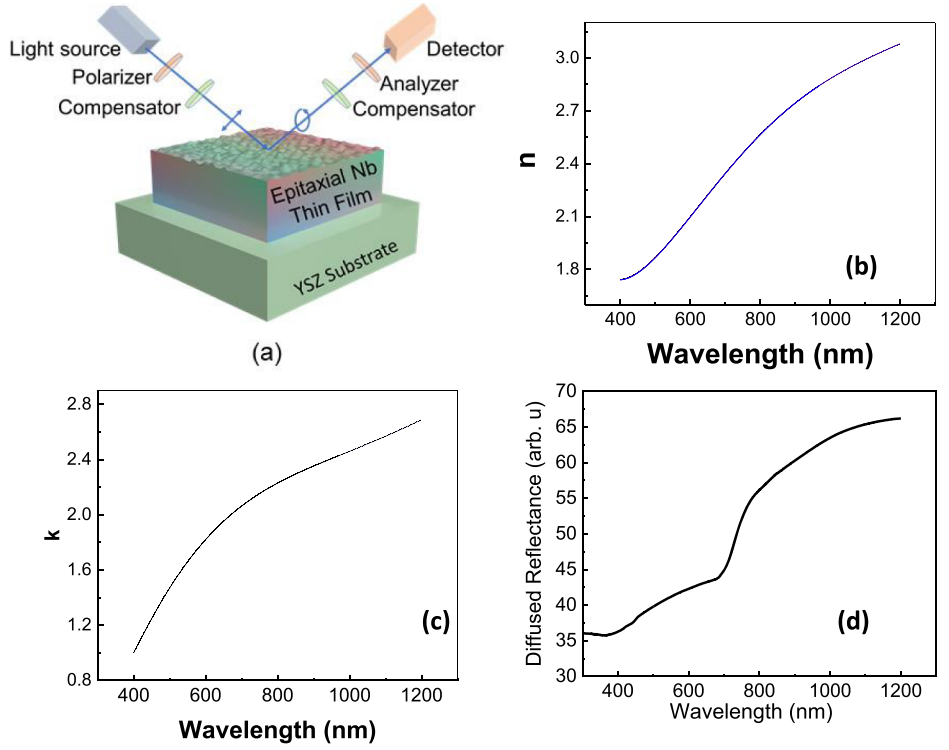

Figure 5. Optical properties of epitaxial Nb films on YSZ substrates. (a) Optical model employed to calculate the optical constants from ellipsometry; (b) spectral dependence of the index of refraction; (c) spectral dependence of k; and (d) diffuse reflectance data.

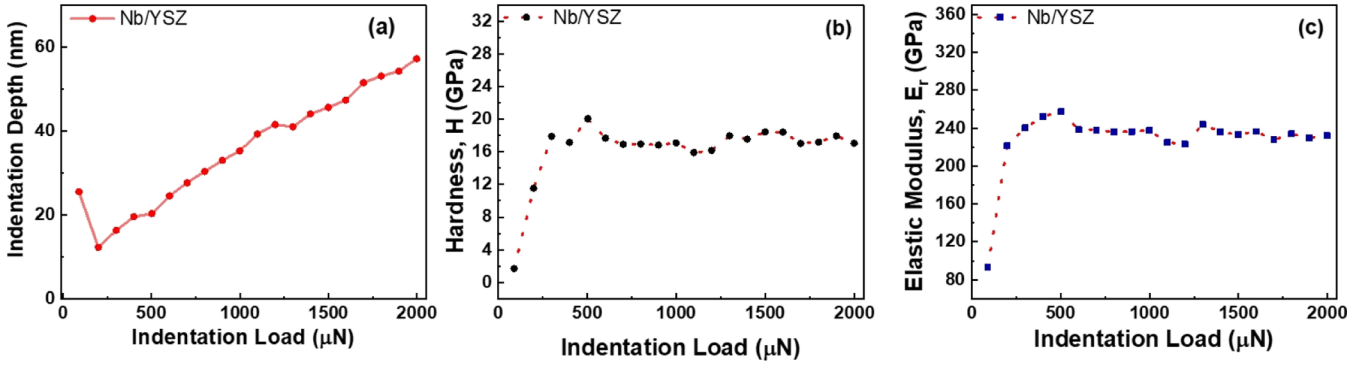

Figure 6. Mechanical characteristics of Nb films deposited on YSZ substrates. (a) Nanoindentation data on Nb films for initial critical load identification; (b) hardness of Nb films as a function of increasing load; and (c) elastic modulus of Nb films as a function of increasing load.

The overall reaction of the heteroepitaxial Nb film under the nonpolarized incident light, with varying frequency, is in good agreement with the reported optical behavior of similar refractory metal-based thin films.[13,14,58] In addition to visible mirror-like reflection, the high reflectivity of the Nb film also indicates the surface quality of the films deposited. We believe that the formation of epitaxial close compact nanocolumnar grains with nanotextured termination at the Nb−air interface influences the reflection pattern and can be tailored precisely by controlling the in situ growth parameters.

For metal thin films, metal−metal interfaces, and metal oxide thin films, the optical constants are sensitive to the crystal structure, morphology, microstructure, defect structure, and chemistry. Most importantly, the surface/interface structure, crystal quality, packing density, lattice parameters, and defect structure of the deposited films strongly influence their optical parameters. Thus, the observed high optical quality noted for Nb films can be attributed to the high structural quality in terms of the epitaxial structure with abrupt interfaces. Usually, the low-packing density and/or defects can result in relatively low values of n and k of the metal films. As reported in the literature, sputtered films can contain a number of impurities, which may be incorporated during deposition from either the residual gas or the sputtering gas. In fact, for comparison with other refractory metallic films, Walker et al.[59] reported that, for a given film thickness, the Mo thin-film samples deposited at lower pressure exhibit higher amplitude imaginary part of the dielectric function at high photon energies which is attributed to the stronger optical absorption associated with the interband transitions. It was found that the lower void volume fraction packing density of crystallites in the films influences the optical properties of Mo films. Also, Wieduwilt et al.[13] used an ultrathin Nb thin film on fiber optical tapers to demonstrate low-loss hybrid plasmonic modes, the refractive index was relatively low than the present report. Therefore, we believe that the n and k values and their

https://doi.org/10.1021/acs.jpcc.1c08738
J. Phys. Chem. C 2022, 126, 2098−2107

dispersion profiles noted in this work are primarily due to the epitaxy, abrupt metal oxide interfaces, and granular morphology coupled with a high structural order within the Nb films deposited on YSZ substrates.

Mechanical Properties. After the detailed characterization of the surface/interface quality, microstructure, and optical properties, the epitaxial Nb films were further inspected with a nanoindentor test to obtain reliable information on their mechanical properties. The mechanical characteristics of the epitaxial Nb films are presented in Figure 6. The first step is to establish an indentation load, where the true characteristics of the films can be obtained. The effect of indentation load on the indentation depth for the case of Nb films is shown in Figure 6a. Epitaxial Nb films clearly exhibit a trend with the indentation depth (Figure 6a), where the indentation load was increased to 2000 μN with increments of 100 μN. The initial set of indentations was believed to be of shallow nature and is mostly on the surface of the Nb-film thickness. However, as we gradually increase the indentation loads, at about 400 μN, the indentation depth is in the range of preferred depth, which is 10−12% of film thickness. Also, the penetration depth follows a linear trend with the increasing indentation load all the way up to 2000 μN.

It is commonly accepted that the underlying substrate dictates the indentation response, particularly for thin films deposited on various substrates. As the depth of indentation increases, the hardness increases correspondingly due to the formation of a plastic zone under the indenter tip.[54] As the plastic zone increases in size and reaches the film−substrate interface, the hardness predominantly comes from the substrate. To better address the mechanical properties of Nb films, the penetration depth of roughly 10% of film thickness was used, as is widely adopted in the literature.[60−62] The hardness and elastic modulus were determined from the load displacement curves.

The variation of hardness and reduced elastic modulus as a function of incremental load up to the peak load of this experiment is shown in Figure 6b. The hardness value reaches a plateau of about ∼18 GPa after a critical load of ∼300 μN. The elastic modulus follows a similar trend, meaning a plateau value is reached with respect to penetration depth (see, Figure 6c). The average hardness and elastic modulus of the Nb epitaxial films were 18 and 240 GPa, respectively. Few existing literature studies are there characterizing nanomechanical properties of Nb thin films on various metallic substrates, such as Pb, stainless steel, and NiTi shape memory alloy.[63−65] Structural characterization showed stabilization of amorphous-polycrystalline mixed-phase Nb thin films. Assertively, hardness and elastic modulus were lower than the current values reported here. We believe that a heteroepitaxially grown Nb thin film on the YSZ substrate, with close compact nanocolumnar single-phase monocrystalline stabilizations, results in exceptional nanomechanical characteristics, still reported.

CONCLUSIONS

We have successfully demonstrated low-temperature heteroepitaxial growth of a compact nanocolumnar Nb thin film with a nanotextured growth front on a YSZ substrate. Atomically smooth Nb−YSZ interface confirms abrupt heterointerfaces at the initial nucleation sites without any back etching or interdiffusion between the substrate and thin film. The exceptionally stable Nb refractory metal, epitaxially grown on a typical substrate, which is known for extreme environment application, is the first demonstration of its kind. It is worth noting that periodical lattice twists develop to compensate the interlayer strain between the substrate and thin film. Corroborated with surface/interface quality, microstructure, and optical properties, the epitaxial Nb films exhibit excellent mechanical characteristics. The hardness and elastic modulus of the Nb epitaxial films were 18 and 240 GPa, respectively, which are attributed primarily to the growth of a compact nanocolumnar Nb epitaxial film on YSZ. The nanoconical top surface could be tuned to further improve the optical behavior of compact nanocolumnar refractory metallic film. As another potential advantage, lower growth temperature is expected to profoundly increase accessibility and widespread integration in many research laboratories. This study opens up the possibility of low-cost heteroepitaxy of metallic thin films and nanostructures on various substrates for high-temperature photonic, plasmonic, and superconducting applications.

AUTHOR INFORMATION

Corresponding Author

C. V. Ramana − *Centre for Advanced Materials Research, University of Texas at El Paso, El Paso, Texas 79968, United States; Department of Mechanical Engineering, University of Texas at El Paso, El Paso, Texas 79968, United States;* orcid.org/0000-0002-5286-3065; Email: rvchintalapalle@utep.edu

Authors

Nanthakishore Makeswaran − *Centre for Advanced Materials Research, University of Texas at El Paso, El Paso, Texas 79968, United States; Department of Mechanical Engineering, University of Texas at El Paso, El Paso, Texas 79968, United States*

Vishal Zade − *Centre for Advanced Materials Research, University of Texas at El Paso, El Paso, Texas 79968, United States; Department of Mechanical Engineering, University of Texas at El Paso, El Paso, Texas 79968, United States*

Debabrata Das − *Centre for Advanced Materials Research, University of Texas at El Paso, El Paso, Texas 79968, United States; Department of Mechanical Engineering, University of Texas at El Paso, El Paso, Texas 79968, United States;* orcid.org/0000-0003-4326-6805

Susheng Tan − *Department of Electrical and Computer Engineering and Petersen Institute of NanoScience and Engineering, University of Pittsburg, Pittsburgh, Pennsylvania 15261, United States;* orcid.org/0000-0002-6162-7443

Shuozhi Xu − *Department of Mechanical Engineering, University of California, Santa Barbara, California 93106-5070, United States*

Irene J. Beyerlein − *Department of Mechanical Engineering, University of California, Santa Barbara, California 93106-5070, United States; Materials Department, University of California, Santa Barbara, California 93016-5050, United States*

Complete contact information is available at: https://pubs.acs.org/10.1021/acs.jpcc.1c08738

Notes

The authors declare no competing financial interest.

ACKNOWLEDGMENTS

The authors acknowledge, with pleasure, support from the National Science Foundation (NSF) with NSF-PREM grant

#DMR-1827745. I.J.B. gratefully acknowledges support from the Office of Naval Research under contract N00014-21-1-2536.

REFERENCES

(1) Suresh, S.; Unni, G. E.; Satyanarayana, M.; Nair, A. S.; Pillai, V. P. M. Ag@Nb_2O_5 plasmonic blocking layer for higher efficiency dye-sensitized solar cells. *Dalton Trans.* **2018**, *47*, 4685−4700.
(2) Yao, J.; Ye, M.; Sun, Y.; Yuan, Y.; Fan, H.; Zhang, Y.; Chen, C.; Liu, C.; Qu, K.; Zhong, G.; et al. Atomic-Scale insight into the reversibility of polar order in ultrathin epitaxial Nb:$SrTiO_3$/$BaTiO_3$ heterostructure and its implication to resistive switching. *Acta Mater.* **2020**, *188*, 23−29.
(3) Kurter, C.; Abrahams, J.; Shvets, G.; Anlage, S. M. Plasmonic scaling of superconducting metamaterials. *Phys. Rev. B: Condens. Matter Mater. Phys.* **2013**, *88*, 180510.
(4) Malureanu, R.; Lavrinenko, A. Ultra-thin films for plasmonics: a technology overview. *Nanotechnol. Rev.* **2015**, *4*, 259−275.
(5) Farag, A.; Ubl, M.; Konzelmann, A.; Hentschel, M.; Giessen, H. Utilizing niobium plasmonic perfect absorbers for tunable near- and mid-IR photodetection. *Opt. Express* **2019**, *27*, 25012−25021.
(6) Kogler, M.; Köck, E.-M.; Bielz, T.; Pfaller, K.; Klötzer, B.; Schmidmair, D.; Perfler, L.; Penner, S. Hydrogen Surface Reactions and Adsorption Studied on Y_2O_3, YSZ, and ZrO_2. *J. Phys. Chem. C* **2014**, *118*, 8435−8444.
(7) Bagheri, S.; Strohfeldt, N.; Ubl, M.; Berrier, A.; Merker, M.; Richter, G.; Siegel, M.; Giessen, H. Niobium as Alternative Material for Refractory and Active Plasmonics. *ACS Photonics* **2018**, *5*, 3298−3304.
(8) Ammal, S. C.; Heyden, A. Combined DFT and Microkinetic Modeling Study of Hydrogen Oxidation at the Ni/YSZ Anode of Solid Oxide Fuel Cells. *J. Phys. Chem. Lett.* **2012**, *3*, 2767−2772.
(9) Mousavi, T.; Hong, Z.; Morrison, A.; London, A.; Grant, P. S.; Grovenor, C.; Speller, S. C. A new approach to fabricate superconducting NbTi alloys. *Supercond. Sci. Technol.* **2017**, *30*, 094001.
(10) Shimizu, Y.; Tonooka, K.; Yoshida, Y.; Furuse, M.; Takashima, H. Growth and superconductivity of niobium titanium alloy thin films on strontium titanate (001) single-crystal substrates for superconducting joints. *Sci. Rep.* **2018**, *8*, 15135.
(11) Shirsath, S. E.; Cazorla, C.; Lu, T.; Zhang, L.; Tay, Y. Y.; Lou, X.; Liu, Y.; Li, S.; Wang, D. Interface-Charge Induced Giant Electrocaloric Effect in Lead Free Ferroelectric Thin-Film Bilayers. *Nano Lett.* **2020**, *20*, 1262−1271.
(12) Ramana, C. V.; Masse, P.; Smith, R. J.; Choi, B. S. Using metallic interlayers to stabilize abrupt, epitaxial metal-metal interfaces. *Phys. Rev. Lett.* **2003**, *90*, 066101.
(13) Wieduwilt, T.; Tuniz, A.; Linzen, S.; Goerke, S.; Dellith, J.; Hübner, U.; Schmidt, M. A. Ultrathin niobium nanofilms on fiber optical tapers - a new route towards low-loss hybrid plasmonic modes. *Sci. Rep.* **2015**, *5*, 17060.
(14) Rashid, H.; Rahman, K. S.; Hossain, M. I.; Nasser, A. A.; Alharbi, F. H.; Akhtaruzzaman, M.; Amin, N. Physical and electrical properties of molybdenum thin films grown by DC magnetron sputtering for photovoltaic application. *Results Phys.* **2019**, *14*, 102515.
(15) Hassan, S. S. A.; Yongbing Xu, X.; Jing Wu, W.; Thompson, S. M. Epitaxial Growth and Magnetic Properties of Half-Metallic Fe_3O_4 on Si(100) Using MgO Buffer Layer. *IEEE Trans. Magn.* **2009**, *45*, 4357−4359.
(16) Clark, E. L.; Ringe, S.; Tang, M.; Walton, A.; Hahn, C.; Jaramillo, T. F.; Chan, K.; Bell, A. T. Influence of Atomic Surface Structure on the Activity of Ag for the Electrochemical Reduction of CO_2 to CO. *ACS Catal.* **2019**, *9*, 4006−4014.
(17) Uekubo, M.; Oku, T.; Nii, K.; Murakami, M.; Takahiro, K.; Yamaguchi, S.; Nakano, T.; Ohta, T. WN_x diffusion barriers between Si and Cu. *Thin Solid Films* **1996**, *286*, 170−175.
(18) Cemin, F.; Lundin, D.; Furgeaud, C.; Michel, A.; Amiard, G.; Minea, T.; Abadias, G. Epitaxial growth of Cu(001) thin films onto Si(001) using a single-step HiPIMS process. *Sci. Rep.* **2017**, *7*, 1655.
(19) Kelso, M. V.; Tubbesing, J. Z.; Chen, Q.; Switzer, J. A. Epitaxial Electrodeposition of Chiral Metal Surfaces on Silicon(643). *J. Am. Chem. Soc.* **2018**, *140*, 15812−15819.
(20) Evans, J. W.; Sanders, D. E.; Thiel, P. A.; DePristo, A. E. Low-temperature epitaxial growth of thin metal films. *Phys. Rev. B: Condens. Matter Mater. Phys.* **1990**, *41*, 5410−5413.
(21) Cheng, C.-W.; Liao, Y.-J.; Liu, C.-Y.; Wu, B.-H.; Raja, S. S.; Wang, C.-Y.; Li, X.; Shih, C.-K.; Chen, L.-J.; Gwo, S. Epitaxial Aluminum-on-Sapphire Films as a Plasmonic Material Platform for Ultraviolet and Full Visible Spectral Regions. *ACS Photonics* **2018**, *5*, 2624−2630.
(22) Cheng, F.; Lee, C.-J.; Choi, J.; Wang, C.-Y.; Zhang, Q.; Zhang, H.; Gwo, S.; Chang, W.-H.; Li, X.; Shih, C.-K. Epitaxial Growth of Optically Thick, Single Crystalline Silver Films for Plasmonics. *ACS Appl. Mater. Interfaces* **2019**, *11*, 3189−3195.
(23) Domask, A. C.; Cooley, K. A.; Kabius, B.; Abraham, M.; Mohney, S. E. Room Temperature van der Waals Epitaxy of Metal Thin Films on Molybdenum Disulfide. *Cryst. Growth Des.* **2018**, *18*, 3494−3501.
(24) Ishibe, T.; Maeda, Y.; Terada, T.; Naruse, N.; Mera, Y.; Kobayashi, E.; Nakamura, Y. Resistive switching memory performance in oxide hetero-nanocrystals with well-controlled interfaces. *Sci. Technol. Adv. Mater.* **2020**, *21*, 195−204.
(25) Ramana, C. V.; Naidu, B. S.; Hussain, O. M.; Pinto, R. Low-temperature growth of vanadium pentoxide thin films produced by pulsed laser ablation. *J. Phys. D: Appl. Phys.* **2001**, *34*, L35−L38.
(26) Nivedita, L. R.; Haubert, A.; Battu, A. K.; Ramana, C. V. Correlation between Crystal Structure, Surface/Interface Microstructure, and Electrical Properties of Nanocrystalline Niobium Thin Films. *Nanomater* **2020**, *10*, 1287.
(27) Varma, S. K.; Sanchez, F.; Moncayo, S.; Ramana, C. V. Static and cyclic oxidation of Nb-Cr-V-W-Ta high entropy alloy in air from 600 to 1400°C. *J. Mater. Sci. Technol.* **2020**, *38*, 189−196.
(28) Tomboc, G. M.; Kwon, T.; Joo, J.; Lee, K. High entropy alloy electrocatalysts: a critical assessment of fabrication and performance. *J. Mater. Chem. A* **2020**, *8*, 14844−14862.
(29) Hori, T.; Nagase, T.; Todai, M.; Matsugaki, A.; Nakano, T. Development of non-equiatomic Ti-Nb-Ta-Zr-Mo high-entropy alloys for metallic biomaterials. *Scr. Mater.* **2019**, *172*, 83−87.
(30) Schuh, B.; Völker, B.; Todt, J.; Schell, N.; Perrière, L.; Li, J.; Couzinié, J. P.; Hohenwarter, A. Thermodynamic instability of a nanocrystalline, single-phase TiZrNbHfTa alloy and its impact on the mechanical properties. *Acta Mater.* **2018**, *142*, 201−212.
(31) Romero, R.; Makeswaran, N.; Naraparaju, R.; Ramana, C. V. Examination of the Oxidation and Metal−Oxide Layer Interface of a Cr−Nb−Ta−V−W High Entropy Alloy at Elevated Temperatures. *Adv. Eng. Mater.* **2021**, *23*, 2100164.
(32) Shibata, Y.; Nomura, S.; Kashiwaya, H.; Kashiwaya, S.; Ishiguro, R.; Takayanagi, H. Imaging of current density distributions with a Nb weak-link scanning nano-SQUID microscope. *Sci. Rep.* **2015**, *5*, 15097.
(33) Yao, D. D.; Rani, R. A.; O'Mullane, A. P.; Kalantar-zadeh, K.; Ou, J. Z. Enhanced Coloration Efficiency for Electrochromic Devices based on Anodized Nb_2O_5/Electrodeposited MoO_3 Binary Systems. *J. Phys. Chem. C* **2014**, *118*, 10867−10873.
(34) Ab Kadir, R.; Rani, R. A.; Alsaif, M. M. Y. A.; Ou, J. Z.; Wlodarski, W.; O'Mullane, A. P.; Kalantar-Zadeh, K. Optical gas sensing properties of nanoporous Nb_2O_5 films. *ACS Appl. Mater. Interfaces* **2015**, *7*, 4751.
(35) Kadir, R. A.; Rani, R. A.; Zoolfakar, A. S.; Ou, J. Z.; Shafiei, M.; Wlodarski, W.; Kalantar-zadeh, K. Nb_2O_5 Schottky based ethanol vapour sensors: Effect of metallic catalysts. *Sens. Actuators, B* **2014**, *202*, 74−82.
(36) Ramana, C. V.; Utsunomiya, S.; Ewing, R. C.; Julien, C. M.; Becker, U. Structural Stability and Phase Transitions in WO_3 Thin Films. *J. Phys. Chem. B* **2006**, *110*, 10430−10435.

https://doi.org/10.1021/acs.jpcc.1c08738
J. Phys. Chem. C 2022, 126, 2098−2107

(37) Martinez, G.; Ramana, C. V. Phase-Control Enabled Superior Mechanical and Electrical Properties of Nanocrystalline Tungsten-Molybdenum Thin Films. *Adv. Eng. Mater.* **2017**, *19*, 1700354.
(38) Battu, A. K.; Zade, V. B.; Deemer, E.; Ramana, C. V. Microstructure-Mechanical Property Correlation in Size Controlled Nanocrystalline Molybdenum Films. *Adv. Eng. Mater.* **2018**, *20*, 1800496.
(39) Clavero, C.; Beringer, D. B.; Roach, W. M.; Skuza, J. R.; Wong, K. C.; Batchelor, A. D.; Reece, C. E.; Lukaszew, R. A. Strain Effects on the Crystal Growth and Superconducting Properties of Epitaxial Niobium Ultrathin Films. *Cryst. Growth Des.* **2012**, *12*, 2588−2593.
(40) Dobrovolskiy, O. V.; Huth, M. Crossover from dirty to clean superconducting limit in dc magnetron-sputtered thin Nb films. *Thin Solid Films* **2012**, *520*, 5985−5990.
(41) Kwo, J.; Hong, M.; Nakahara, S. Growth of rare-earth single crystals by molecular beam epitaxy: The epitaxial relationship between hcp rare earth and bcc niobium. *Appl. Phys. Lett.* **1986**, *49*, 319−321.
(42) Petrucci, M.; Pitt, C. W.; Reynolds, S. R.; Milledge, H. J.; Mendelssohn, M. J.; Dineen, C.; Freeman, W. G. Growth of thin-film niobium and niobium oxide layers by molecular-beam epitaxy. *J. Appl. Phys.* **1988**, *63*, 900−909.
(43) Wildes, A. R.; Theis-Bröhl, K. The growth and structure of epitaxial niobium on sapphire. *Thin Solid Films* **2001**, *401*, 7−34.
(44) Beringer, D. B.; Roach, W. M.; Clavero, C.; Reece, C. E.; Lukaszew, R. A. Characterization of two different orientations of epitaxial niobium thin films grown on MgO(001) surfaces. *J. Appl. Phys.* **2013**, *114*, 223502.
(45) Milosevic, E.; Kerdsongpanya, S.; McGahay, M. E.; Wang, B.; Gall, D. The Resistivity Size Effect in Epitaxial Nb(001) and Nb(011) Layers. *IEEE Trans. Electron Devices* **2019**, *66*, 3473−3478.
(46) Stolze, K.; Tao, J.; von Rohr, F. O.; Kong, T.; Cava, R. J. Sc−Zr−Nb−Rh−Pd and Sc−Zr−Nb−Ta−Rh−Pd High-Entropy Alloy Superconductors on a CsCl-Type Lattice. *Chem. Mater.* **2018**, *30*, 906−914.
(47) Campo, L. d.; De Sousa Meneses, D.; Wittmann-Ténèze, K.; Bacciochini, A.; Denoirjean, A.; Echegut, P. Effect of Porosity on the Infrared Radiative Properties of Plasma-Sprayed Yttria-Stabilized Zirconia Ceramic Thermal Barrier Coatings. *J. Phys. Chem. C* **2014**, *118*, 13590−13597.
(48) do Rosário, J. J.; Dyachenko, P. N.; Kubrin, R.; Pasquarelli, R. M.; Petrov, A. Y.; Eich, M.; Schneider, G. A. Facile deposition of YSZ-inverse photonic glass films. *ACS Appl. Mater. Interfaces* **2014**, *6*, 12335−12345.
(49) Chang, C.-H.; Hsia, B.; Alper, J. P.; Wang, S.; Luna, L. E.; Carraro, C.; Lu, S.-Y.; Maboudian, R. High-Temperature All Solid-State Microsupercapacitors based on SiC Nanowire Electrode and YSZ Electrolyte. *ACS Appl. Mater. Interfaces* **2015**, *7*, 26658−26665.
(50) Makeswaran, N.; Battu, A. K.; Deemer, E.; Ramana, C. V. Crystal Growth and Structure−Property Optimization of Thermally Annealed Nanocrystalline Ga_2O_3 Films. *Cryst. Growth Des.* **2020**, *20*, 2893−2903.
(51) Gutierrez, G.; Sundin, E. M.; Nalam, P. G.; Zade, V.; Romero, R.; Nair, A. N.; Sreenivasan, S.; Das, D.; Li, C.; Ramana, C. V. Interfacial Phase Modulation-Induced Structural Distortion, Band Gap Reduction, and Nonlinear Optical Activity in Tin-Incorporated Ga_2O_3. *J. Phys. Chem. C* **2021**, *125*, 20468−20481.
(52) Zade, V.; Makeswaran, N.; Boyce, B. L.; Paraguay-Delgado, F.; Ramana, C. V. Structural and mechanical properties of nanocrystalline Ga_2O_3 films made by pulsed laser deposition onto transparent quartz substrates. *Nano Express* **2021**, *2*, 020006.
(53) Hussein, M.; Kumar, M.; Drew, R.; Al-Aqeeli, N. Electrochemical Corrosion and In Vitro Bioactivity of Nano-Grained Biomedical Ti-20Nb-13Zr Alloy in a Simulated Body Fluid. *Materials* **2017**, *11*, 26.
(54) Nix, W. D. Mechanical Properties of Thin Films. *Metall. Trans. A* **1989**, *20*, 2217.
(55) Mills, E. M.; Kleine-Boymann, M.; Janek, J.; Yang, H.; Browning, N. D.; Takamura, Y.; Kim, S. YSZ thin films with minimized grain boundary resistivity. *Phys. Chem. Chem. Phys.* **2016**, *18*, 10486−10491.
(56) Mühlenbein, L.; Bhal Singh, C.; Hähnel, A.; Campbell, S.; Hagendorf, C.; Bhatnagar, A. Impact of Samarium on the Growth of Epitaxial Bismuth Ferrite Thin Films. *Phys. Status Solidi B* **2020**, *257*, 1900625.
(57) Makeswaran, N.; Das, D.; Zade, V.; Gaurav, P.; Shutthanandan, V.; Tan, S.; Ramana, C. V. Size-and Phase-Controlled Nanometer-Thick β-Ga_2O_3 Films with Green Photoluminescence for Optoelectronic Applications. *ACS Appl. Nano Mater.* **2021**, *4*, 3331−3338.
(58) Chen, H.-P.; Lee, C.-T.; Liao, W.-B.; Chang, Y.-C.; Chen, Y.-S.; Li, M.-C.; Lee, C.-C.; Kuo, C.-C. Analysis of High-Efficiency Mo-Based Solar Selective Absorber by Admittance Locus Method. *Coatings* **2019**, *9*, 256.
(59) Walker, J. D.; Khatri, H.; Ranjan, V.; Li, J.; Collins, R. W.; Marsillac, S. Electronic and structural properties of molybdenum thin films as determined by real-time spectroscopic ellipsometry. *Appl. Phys. Lett.* **2009**, *94*, 141908.
(60) Battu, A. K.; Manandhar, S.; Ramana, C. V. Nanomechanical characterization of titanium incorporated gallium oxide nanocrystalline thin films. *Mater. Today Nano* **2018**, *2*, 7−14.
(61) Battu, A. K.; Manandhar, S.; Shutthanandan, V.; Ramana, C. V. Controlled optical properties via chemical composition tuning in molybdenum-incorporated β-Ga_2O_3 nanocrystalline films. *Chem. Phys. Lett.* **2017**, *684*, 363−367.
(62) Battu, A. K.; Ramana, C. V. Mechanical properties of nanocrystalline and amorphous gallium oxide thin films. *Adv. Eng. Mater.* **2018**, *20*, 1701033.
(63) Khamseh, S.; Alibakhshi, E.; Ramezanzadeh, B.; Ganjaee Sari, M. A tailored pulsed substrate bias voltage deposited (a-C: Nb) thin-film coating on GTD-450 stainless steel: Enhancing mechanical and corrosion protection characteristics. *Chem. Eng. J.* **2021**, *404*, 126490.
(64) Seifried, F.; Leiste, H.; Schwaiger, R.; Ulrich, S.; Seifert, H. J.; Stueber, M. Structure, morphology and selected mechanical properties of magnetron sputtered (Mo, Ta, Nb) thin films on NiTi shape memory alloys. *Surf. Coat. Technol.* **2018**, *347*, 379−389.
(65) Gontad, F.; Lorusso, A.; Panareo, M.; Monteduro, A. G.; Maruccio, G.; Broitman, E.; Perrone, A. Nanomechanical and electrical properties of Nb thin films deposited on Pb substrates by pulsed laser deposition as a new concept photocathode for superconductor cavities. *Nucl. Instrum. Methods Phys. Res., Sect. A* **2015**, *804*, 132−136.

https://doi.org/10.1021/acs.jpcc.1c08738
J. Phys. Chem. C 2022, 126, 2098−2107